

Itinerant G-type antiferromagnet SrCr₂As₂ studied by magnetization, heat capacity, electrical resistivity, and NMR measurements

Q.-P. Ding ^{1,2}, Santanu Pakhira ¹, N. S. Sangeetha ^{1,*}, E. H. Krenkel ^{1,2}, E. I. Timmons ^{1,2}, M. A. Tanatar ^{1,2},
R. Prozorov ^{1,2}, D. C. Johnston ^{1,2} and Y. Furukawa ^{1,2}

¹Ames Laboratory, Iowa State University, Ames, Iowa 50011, USA

²Department of Physics and Astronomy, Iowa State University, Ames, Iowa 50011, USA



(Received 8 September 2021; revised 9 March 2022; accepted 25 March 2022; published 8 April 2022)

The physical properties of itinerant antiferromagnetic (AFM) SrCr₂As₂ with body-centered tetragonal ThCr₂Si₂ structure were investigated in single crystalline and polycrystalline forms by electrical resistivity ρ , heat capacity C_p , magnetic susceptibility χ versus temperature T , and magnetization M versus applied magnetic field H isotherm measurements as well as ⁷⁵As and ⁵³Cr nuclear magnetic resonance (NMR) measurements in the wide temperature range $T = 1.6\text{--}900$ K. From the $\chi(T)$ and ⁷⁵As NMR measurements, the G-type AFM state below $T_N = 615(15)$ K has been determined, consistent with the previous neutron-diffraction measurements. Direct evidence of magnetic ordering of the Cr spins was shown by the observation of the ⁵³Cr NMR spectrum under $H = 0$. From the $\chi(T)$ measurements on single-crystal SrCr₂As₂ under the two different magnetic field directions $H \parallel ab$ and $H \parallel c$ in the AFM state, the Cr ordered moments are shown to align along the c axis in the G-type AFM state. The metallic state is directly evidenced by the ρ , C_p , and NMR measurements, and the density of states at the Fermi energy $\mathcal{D}(E_F)$ in the AFM state is estimated to be 7.53 states/eV f.u. for both spin directions which is almost twice the bare $\mathcal{D}(E_F)$ estimated from first-principles calculations, suggesting an enhancement of the conduction-carrier mass by a factor of two in the AFM state. The $\mathcal{D}(E_F)$ is found to be nearly constant below at least 100 K and is independent of H . The $\rho(T)$ is found to show T -linear behavior above T_N and exhibits positive curvature below T_N where significant loss of spin-disorder scattering upon magnetic ordering is observed. The resistivity anisotropy of the compound remains moderate $\rho_c/\rho_a \sim 9$ through most of the magnetically ordered phase but shows a rapid increase below 50 K.

DOI: [10.1103/PhysRevB.105.134408](https://doi.org/10.1103/PhysRevB.105.134408)

I. INTRODUCTION

Since the discovery of high T_c superconductivity in iron pnictides [1], the interplay between electron correlations and unconventional superconductivity (SC) has attracted much interest. In most of the Fe-based superconductors (FBSC), the parent materials are metallic and exhibit antiferromagnetic (AFM) ordering below the Néel temperature T_N [2–4]. SC in these compounds emerges upon suppression of the AFM phase by the application of pressure and/or chemical substitution. Because of the proximity between the magnetically ordered and SC phases, the effects of electron correlations on the appearance of SC are naturally considered to be important.

The role of the electron correlations can be investigated by varying the $3d$ transition-metal elements since electron correlations could be caused by strong Hund's exchange interactions for $3d$ electrons. In the case of $3d^5$ configurations, the half-filled $3d$ electron shells will lead to a Mott insulating state. For example, an insulating state is observed in BaMn₂As₂ [Mn²⁺ ($S = 5/2$, $3d^5$)] which exhibits an AFM state below a high Néel temperature $T_N = 625$ K [5,6]. For FBSCs such as AFe₂As₂ ($A = \text{Sr, Ba, Ca}$), a nearly $3d^6$ electron configuration ($S = 2$) is expected for the Fe ions in the

metallic state. On the other hand, $3d^4$ electron configurations are expected for Cr²⁺ ions in Cr-based compounds such as A²⁺Cr₂As₂. This is an interesting system since a $3d^4$ electron configuration ($S = 2$) can be considered as a mirror of the $3d^6$ electron configuration for Fe²⁺ ions in the parent materials of FBSC such as A²⁺Fe₂As₂ with respect to the $3d^5$ electron configuration.

Recent theoretical proposals for the possible appearance of superconductivity in Cr-based compounds such as electron-doped LaOCrAs [7,8] and negative-pressurized and/or electron-doped BaCr₂As₂ [9] as well as the discovery of SC in CrAs under pressure [10,11], and in A₂Cr₃As₃ ($A = \text{Na, K, Rb, Cs}$) [12–15] and ACr₃As₃ ($A = \text{K, Rb}$) [16] also lead to further interest in investigating Cr-based compounds. BaCr₂As₂, one of the ACr₂As₂ systems with the body-centered tetragonal ThCr₂Si₂-type structure, is a metallic G-type antiferromagnet with a Néel temperature $T_N \sim 580(10)$ K with a Cr ordered moment of $1.9 \mu_B/\text{Cr}$ aligned along the c axis [17]. A reduction in electron correlations in BaCr₂As₂ in comparison with the half-filled $3d^5$ case has been reported from angle-resolved photoemission spectroscopy (ARPES) measurements [18,19], where a stronger Cr-As covalency relative to the Fe-based SCs was suggested to be an important factor in the appearance of SC. The isostructural compound SrCr₂As₂ has been reported to exhibit the same G-type AFM ordering with Cr ordered moments $1.9 \mu_B/\text{Cr}$ (see Fig. 1) below $T_N = 590(5)$ K from neutron

*Present address: Institute for Experimental Physics IV, Ruhr University Bochum, 44801 Bochum, Germany.

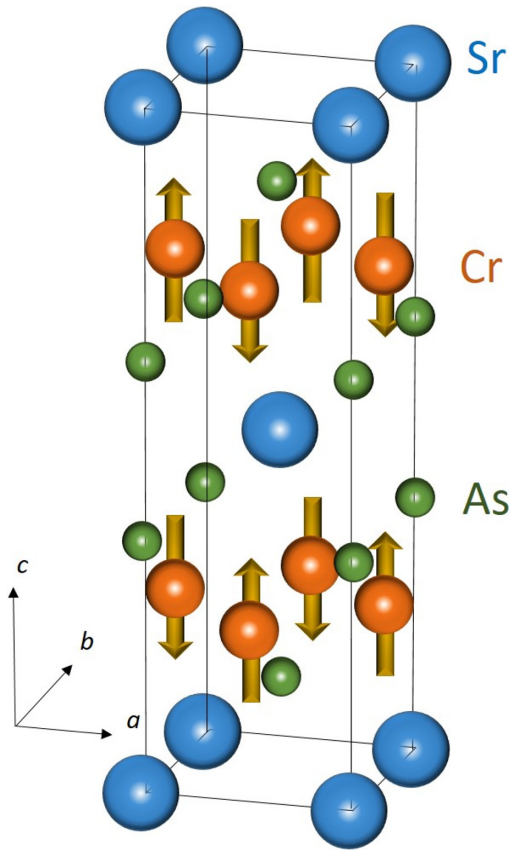


FIG. 1. Crystal and G-type magnetic structures of SrCr_2As_2 . The arrows represent the direction of the Cr ordered moments in the antiferromagnetic state. After Ref. [20].

diffraction (ND) and magnetic susceptibility versus temperature $\chi(T)$ measurements on polycrystalline samples [20]. Although the reduction of the Cr ordered moments of $1.9 \mu_{\text{B}}/\text{Cr}$ from $4 \mu_{\text{B}}/\text{Cr}$ expected for a localized state of Cr^{2+} ion in SrCr_2As_2 suggests an itinerant nature [20], there is no direct experimental evidence of a metallic state in the compound.

No electrical resistivity $\rho(T)$ study has been reported on SrCr_2As_2 in either polycrystalline or single crystalline forms. Even for the isostructural compound BaCr_2As_2 , little is known about the behavior of $\rho(T)$. In-plane resistivity measurements were made up to 300 K in BaCr_2As_2 [17,19], and found a notably nonlinear temperature dependence. Because of the high magnetic ordering temperature ~ 600 K, these measurements merely cover half of T_{N} . The resistivity change through the magnetic transition provides an important insight into the changes of the Fermi surface due to magnetic superzone boundaries and the contribution of magnetic scattering, so getting this information is important. In addition, there is no information on the anisotropy of $\rho(T)$ in these compounds. Therefore it is important to obtain the information of not only in-plane but also interplane $\rho(T)$ up to higher temperature above T_{N} in SrCr_2As_2 . Furthermore, no measurements such as heat capacity C_p and magnetization M versus applied magnetic field H isotherm measurements to characterize the physical properties of SrCr_2As_2 have been reported so far, although recently a Raman spectroscopy study on single crystalline SrCr_2As_2 has been performed [21].

In this paper, we report a comprehensive study of both polycrystalline and single crystalline SrCr_2As_2 in a wide temperature range from 1.6 to 900 K from ρ , M , C_p and nuclear magnetic resonance (NMR) measurements. After the description of the experimental details in Sec. II, we first show the results of x-ray diffraction measurements on a polycrystalline sample in Sec. III A. Then the results of $\chi(T)$ and $M(H)$ measurements are reported in Sec. III B. In Sec. III C, the $C_p(T)$ data are presented. The results of the in-plane and interplane electrical resistivities of SrCr_2As_2 are discussed in Sec. III D. The results of ^{75}As and ^{53}Cr NMR measurements are shown in Sec. III E. Finally summary of our results is given in Sec. IV.

II. EXPERIMENTAL DETAILS

A polycrystalline sample of SrCr_2As_2 was prepared by conventional solid-state reaction using high-purity Sr (Sigma Aldrich, 99.95%), Cr (Alfa Aesar, 99.99%) and As (Alfa Aesar, 99.999 99%). Dendritic Sr pieces were taken with prereacted CrAs in the molar ratio $\text{Sr}:\text{CrAs} = 1.05:2$. The additional amount of Sr was to compensate for the loss of Sr due to evaporation and to reduce the presence of CrAs impurity phase. The Sr and CrAs mixture was pelletized and loaded into an alumina crucible followed by sealing in an evacuated silica tube under $\approx 1/4$ atm of high-purity Ar gas. The assembly was then heated to 900°C at the rate of $100^\circ\text{C}/\text{h}$ and held there for 48 h followed by furnace cooling to room temperature. The heat-treated pellet was then reground inside a He-filled glove box and pelletized again for an additional heat treatment as just described. In order to ensure homogeneous phase formation, this process was repeated once more with intermediate grinding. Finally, the sample was heated to 1150°C at a rate of $100^\circ\text{C}/\text{h}$ and annealed there for 48 h followed by furnace cooling.

Room-temperature powder x-ray diffraction (XRD) measurements on the powdered polycrystalline sample were carried out using a Rigaku Geigerflex x-ray diffractometer with $\text{Cu-K}\alpha$ radiation. Structural analysis was performed by Rietveld refinement using the FULLPROF software package [22].

Single crystals of SrCr_2As_2 were grown by the solution-growth technique using Sn flux with a molar ratio $\text{Sr}:\text{Cr}:\text{As}:\text{Sn} = 1.1:2:2:10$. The starting elements described above were loaded into an alumina crucible which was then sealed in a silica tube under $\approx 1/4$ atm of high-purity Ar gas. The sealed tube was then heated to 600°C at a rate of $50^\circ\text{C}/\text{h}$ where the temperature was held for 6 h. The temperature was then ramped to 1100°C at a rate of $100^\circ\text{C}/\text{h}$ and held there for 20 h. The assembly was then cooled to 500°C at a rate of $3^\circ\text{C}/\text{h}$ where it was centrifuged to remove the crystals from the remaining flux. Shiny crystal plates with typical dimensions $2 \times 2 \times 0.2 \text{ mm}^3$ were obtained.

The chemical composition and homogeneity of the crystals were checked using a JEOL scanning-electron microscope (SEM) equipped with an energy-dispersive x-ray spectroscopy (EDS) analyzer. M measurements were carried out using a Magnetic Property Measurement System from Quantum Design, Inc., in the T range 1.8–300 K and with H up to 5.5 T ($1 \text{ T} \equiv 10^4 \text{ Oe}$). The high-temperature M measurements

from 300 to 900 K were performed using the vibrating-sample magnetometer option for a Physical Property Measurement System (PPMS, Quantum Design, Inc.). The C_p and four-probe ρ measurements were carried out using the PPMS. The $C_p(H, T)$ was measured using a relaxation technique.

Samples for resistivity study were prepared from thin slabs, cleaved out of the crystal with two fresh surfaces corresponding to the tetragonal ab plane. For four-probe in-plane resistivity measurements, the bar-shaped samples were cleaved with the long side corresponding to the tetragonal a axis with typical dimensions $2 \times 0.3 \times 0.05$ mm³. For measurements in the range 1.8 to 400 K, contacts to the samples were prepared by soldering 50- μ m diameter silver wires using tin as solder, a technique also used for creating contacts to iron-based superconductors [23–25]. The contact resistance for SrCr₂As₂-Sn contacts turned out to be similarly low, several $\mu\Omega$, enabling two-probe interplane c -axis resistivity measurements (see Refs. [23,26] for details). The samples for interplane resistivity measurements were plate-shaped (typically 0.05 mm thick with 0.5×0.5 mm² area) and their top and bottom surfaces were covered with Sn and two silver wires attached acting as current and voltage probes in the four-probe resistivity measurements. The actual resistance measured in this experiment is a sum of sample and contact resistances, with the contact resistance representing approximately 1% of the measured resistance. Measurements in samples with the length along the current path significantly smaller than the cross-sectional dimensions suffer grossly from internal sample connectivity. Because of this, measurements were performed on more than 20 samples to verify reproducibility.

Whereas the PPMS measurements were performed in the temperature range 1.8 to 400 K, high-temperature resistivity measurements up to 700 K were performed in a homemade fixture placed in a vacuum furnace. A platinum resistance thermometer PT-100 was used for temperature readings. Contacts to the sample were made with conducting silver paste, with typical contact resistances in the 1- Ω range. Four-probe resistivity measurements were made using an LS372 resistance bridge. For the sake of comparison we measured the resistivity of a nickel wire in the same home-made furnace setup. The wire was of 99.95% purity from Alfa Aesar. We found reasonable coincidence of the ferromagnetic transition temperature with the literature data [27], confirming the accuracy of the temperature readings (see the left inset in Fig. 8 below).

NMR measurements of ⁷⁵As ($I = \frac{3}{2}$, $\frac{\gamma_N}{2\pi} = 7.2919$ MHz/T, $Q = 0.29$ barns) and ⁵³Cr ($I = \frac{3}{2}$, $\frac{\gamma_N}{2\pi} = 2.40664$ MHz/T, $Q = 0.03$ barns) nuclei were conducted using a laboratory-built phase-coherent spin-echo pulse spectrometer in a wide temperature range 1.6–630 K. For $T \geq 300$ K, ⁷⁵As NMR spectra were measured in steps of resonance frequency f by measuring the intensity of the Hahn spin echo at $H = 7.4089$ T. For $T \leq 300$ K, ⁷⁵As NMR spectra were obtained by sweeping H at a fixed frequency $f = 51.1$ MHz. The ⁵³Cr NMR spectrum at $T = 1.6$ K was measured in steps of f by measuring the intensity of the Hahn spin echo at $H = 0$. The ⁷⁵As nuclear spin-lattice relaxation rate $1/T_1$ was measured with a saturation-recovery method. $1/T_1$ at each T

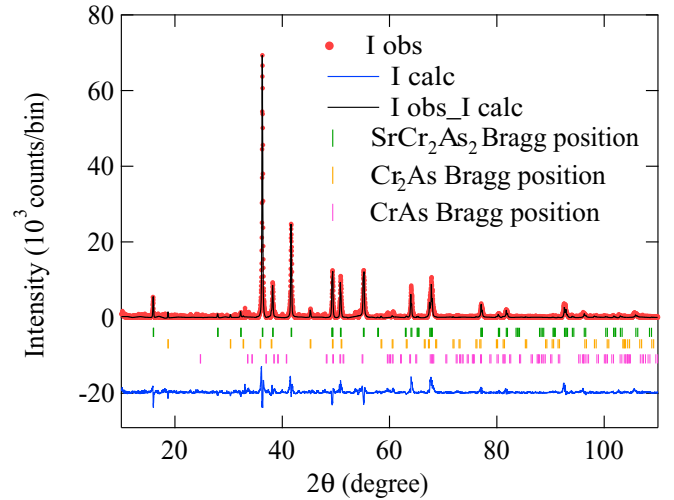


FIG. 2. X-ray diffraction pattern for polycrystalline SrCr₂As₂ obtained using a Rigaku powder diffractometer and Cu- K_α radiation. The observed data are shown by filled red circles, the allowed Bragg diffraction positions as vertical green bars, Cr₂As impurity peaks as vertical orange bars, CrAs impurity peaks as vertical pink bars, the three-phase fit by the black curve, and the difference between the observed data and the two-phase refinement as the bottom blue trace.

was determined by fitting the nuclear magnetization M versus time t using the exponential function $1 - M(t)/M(\infty) = 0.1e^{-t/T_1} + 0.9e^{-6t/T_1}$, where $M(t)$ and $M(\infty)$ are the nuclear magnetization at time t after saturation and the equilibrium nuclear magnetization at $t \rightarrow \infty$, respectively.

III. RESULTS AND DISCUSSION

A. Structural characterization

The room-temperature XRD pattern of the polycrystalline SrCr₂As₂ sample is shown in Fig. 2. The intense peaks could be indexed with the ThCr₂Si₂-type crystal structure with lattice parameters $a = b = 3.87(4)$ Å and $c = 12.89(2)$ Å. For comparison, previously reported room-temperature lattice parameters are $a = 3.918(3)$ Å and $c = 13.05(1)$ Å [28]. The additional contributions to the x-ray diffraction pattern from minor amounts of CrAs (1.0 wt%) and Cr₂As (5.3 wt%) are shown by the three-phase refinement in Fig. 2. However, the magnetic contributions from these two impurity phases are negligible and do not alter the observed intrinsic magnetic behavior of polycrystalline SrCr₂As₂ as reported earlier using neutron diffraction measurements [20]. The SEM-EDS measurements of the single crystals revealed good homogeneity with the average composition SrCr_{2.03(2)}As_{2.04(4)}.

B. Magnetic susceptibility and isothermal magnetization versus magnetic field measurements

The T dependence of the zero-field-cooled (ZFC) magnetic susceptibility $\chi = M/H$ for polycrystalline SrCr₂As₂ measured in different magnetic fields is shown in Fig. 3(a). There is no evidence for the first-order antiferromagnetic/paramagnetic transition in the CrAs impurity phase [29,30] at 258 K. In addition, the direction-averaged χ of CrAs is

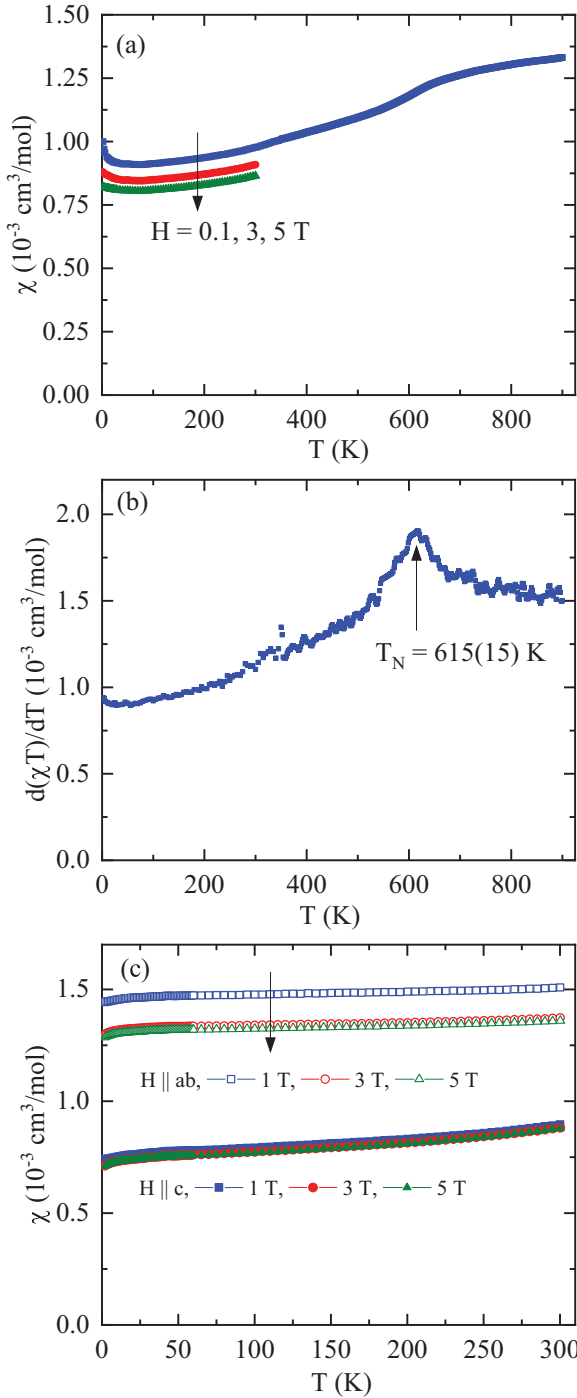


FIG. 3. (a) Temperature T dependence of the magnetic susceptibility $\chi = M/H$ for polycrystalline SrCr_2As_2 measured at different magnetic fields H . The low- T upturns are likely associated with minor amounts of paramagnetic impurities that are suppressed at the higher fields. (b) $d(\chi T)/dT$ vs T obtained using the data for $H = 0.1 \text{ T}$ in (a). The peak in the plot gives the Néel temperature [31] $T_N = 615(15) \text{ K}$ as indicated by an arrow. (c) Anisotropy in $\chi(T)$ for a SrCr_2As_2 crystal measured at different fields for both $H \parallel ab$ and $H \parallel c$.

only ≈ 5.5 and $7.4 \times 10^{-4} \text{ cm}^3/\text{mol}$ for $T \rightarrow 0$ and 300 K , respectively [30], which when multiplied by the small CrAs fraction of the sample is small compared to the measured

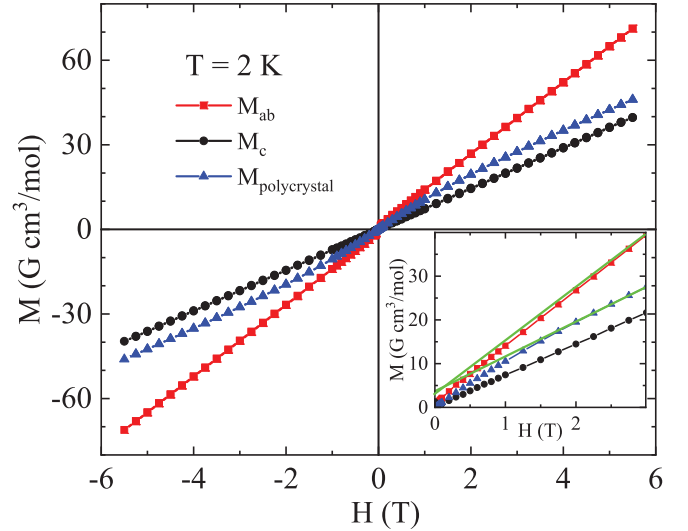


FIG. 4. Four-quadrant $M(H)$ hysteresis loops measured at $T = 2 \text{ K}$ for single crystalline SrCr_2As_2 in two field directions and for polycrystalline SrCr_2As_2 . Inset: Expanded low- H region where the same weak nonlinearity is observed for the polycrystalline sample and in $M_{ab}(H)$ for the single crystal. Extrapolation of the higher-field data to $H = 0$ (solid green lines) gives a FM or PM impurity magnetization of $\sim 3 \text{ G cm}^3/\text{mol} = 0.0005 \mu_B/\text{f.u.}$ for both the polycrystalline and single-crystal samples.

polycrystalline data in Fig. 3(a). Additionally, the $\chi(T)$ data exhibit a small upturn below $\approx 35 \text{ K}$ that is likely due to the contribution of paramagnetic (PM) impurities. This contribution tends to saturate at high H as expected.

A plot of $d(\chi T)/dT$ versus T obtained from the data for $H = 0.1 \text{ T}$ in Fig. 3(a) is shown in Fig. 3(b). The peak in this plot (the Fisher relation [31]) gives the Néel temperature $T_N = 615(15) \text{ K}$. This value agrees with $T_N = 590(5) \text{ K}$ obtained in previous ND measurements of SrCr_2As_2 which also showed that the ordering of the itinerant Cr moments is G-type with the moments aligned along the tetragonal c axis [20]. The broad increase in $\chi(T)$ for $T > T_N$ in Fig. 3(a) is characteristic of two-dimensional AFM correlations persisting well above T_N in this itinerant antiferromagnet, similar to previous reports for the 122-type local-moment pnictide insulators SrMn_2As_2 , CaMn_2As_2 , SrMn_2Sb_2 , SrMn_2P_2 , and SrMn_2P_2 [32–34].

Figure 3(c) shows the ZFC $\chi(T)$ data of a SrCr_2As_2 single crystal in the T range $2\text{--}300 \text{ K}$ measured at different fields applied in the ab plane (χ_{ab}) and along the c axis (χ_c). The $\chi(T)$ data are strongly anisotropic with $\chi_{ab} > \chi_c$ and χ_{ab} shows a weak T dependence, as expected for a collinear antiferromagnet with c -axis moment alignment. The field-dependent anisotropy of χ_{ab} is likely due to a trace amount of ferromagnetic (FM) or PM impurity as discussed below. The $\chi_c(T)$ is also discussed below.

$M(H)$ hysteresis loops measured at $T = 2 \text{ K}$ for polycrystalline and single-crystal SrCr_2As_2 are shown in Fig. 4. No magnetic hysteresis is found in either form of the material for either field direction. However, a weak negative curvature in the low-field $M(H)$ data for the polycrystalline sample and the $M_{ab}(H)$ data for the single crystal is observed (inset of Fig. 4),

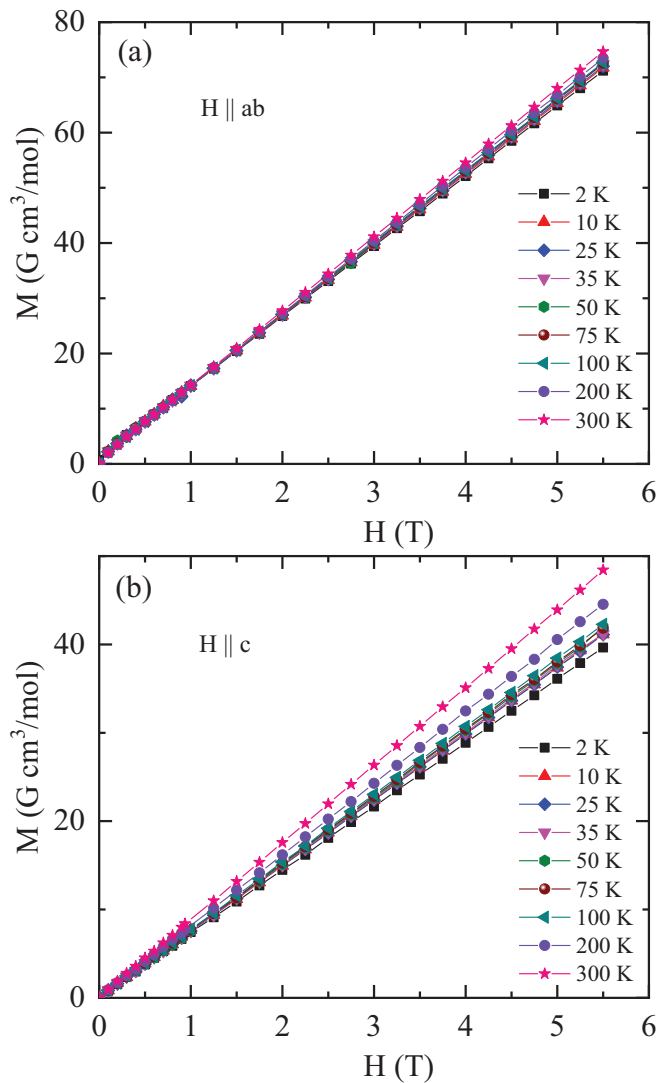


FIG. 5. $M(H)$ isotherms for a SrCr_2As_2 single crystal at different temperatures for (a) $H \parallel ab$ and (b) $H \parallel c$.

which is likely associated with the contribution of FM or of PM impurities detected in the above $\chi(T)$ measurements. At higher fields this contribution saturates. The saturation magnetization of the impurities is estimated by extrapolating the linear high-field $M(H)$ data to $H = 0$ and is found to be only $\approx 3 \text{ G cm}^3/\text{mol} \approx 0.0005 \mu_B/\text{f.u.}$, where μ_B is the Bohr magneton and f.u. means formula unit.

Figures 5(a) and 5(b) show $M(H)$ isotherms of single-crystal SrCr_2As_2 measured at different temperatures for $H \parallel ab$ and $H \parallel c$, respectively. The $M(H)$ data for $H \parallel ab$ are almost independent of T , whereas that for $H \parallel c$ is weakly T dependent, consistent with the $\chi(T)$ data in Fig. 3(c).

According to the first-principles calculations in Ref. [35], the magnetocrystalline anisotropy energy (MAE) favors c -axis moment alignment by an amount

$$\text{MAE}([001] - [100]) = -0.20 \text{ meV/Cr atom}, \quad (1)$$

consistent with the c -axis AFM ordering. Taking the observed ordered moment $\mu = 1.9 \mu_B/\text{Cr atom}$ from Ref. [20], in a c -axis magnetic field the spin-flop transition field H_{SF} at $T =$

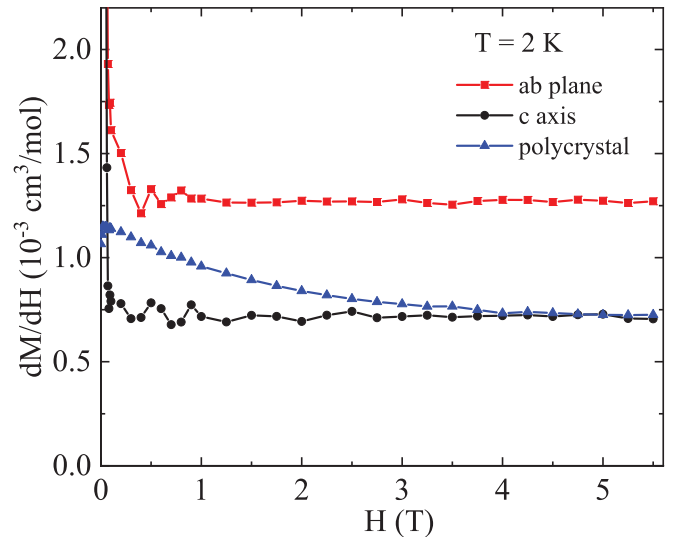


FIG. 6. Field derivative dM/dH vs H obtained from the $M(H)$ data at $T = 2 \text{ K}$ for SrCr_2As_2 in Fig. 4.

0 is calculated to be

$$H_{\text{SF}} = \frac{\text{MAE}}{\mu} = 1.8 \text{ T}. \quad (2)$$

The $M(H, T = 2 \text{ K})$ data for $H \parallel c$ in Fig. 5(b) show no evidence for a spin-flop transition at this field. To look for a small anomaly at this field, Fig. 6 shows a plot of $dM(H)/dH$ versus H at $T = 2 \text{ K}$ and no evidence of a transition at 1.8 T is seen. This indicates no spin-flop transition at least up to 5.5 T, suggesting that the MAE is greater than $|-0.61| \text{ meV/Cr atom}$ based on Eq. (2). The difference between the observed and the calculated values is important for further theoretical investigation. As shown above, the $M(H, T = 2 \text{ K})$ data for $H \parallel c$ have a nonzero slope and the $\chi_c(T)$ data in Fig. 3(c) are nonzero, contrary to the expectation of $\chi_c(T \rightarrow 0) = 0$ for a collinear c -axis antiferromagnet. In addition, we note that if the Cr moments are considered to be point dipoles, the magnetic ordering direction from the magnetic-dipole interaction would be in the ab plane instead of along the c axis [36]. These differences from expectation for a local-moment system likely originate from the itinerant nature of the magnetism in SrCr_2As_2 .

C. Heat capacity measurements

The zero-field heat capacity $C_p(T)$ of single-crystal SrCr_2As_2 for $T = 1.8\text{--}300 \text{ K}$ is plotted in Fig. 7. The C_p attains a value of $\approx 121 \text{ J/mol K}$ at $T = 300 \text{ K}$, which is close to the classical Dulong-Petit high- T limit $C_V = 3nR = 124.71 \text{ J/mol K}$ associated with acoustic lattice-vibration modes, where $n = 5$ is the number of atoms per formula unit and R is the molar-gas constant. The bump observed at $T \approx 290 \text{ K}$ in $C_p(T)$ is due to melting of the Apiezon N-grease used for making thermal contact between the crystal and sample platform of the heat capacity puck and is hence an instrumental artifact.

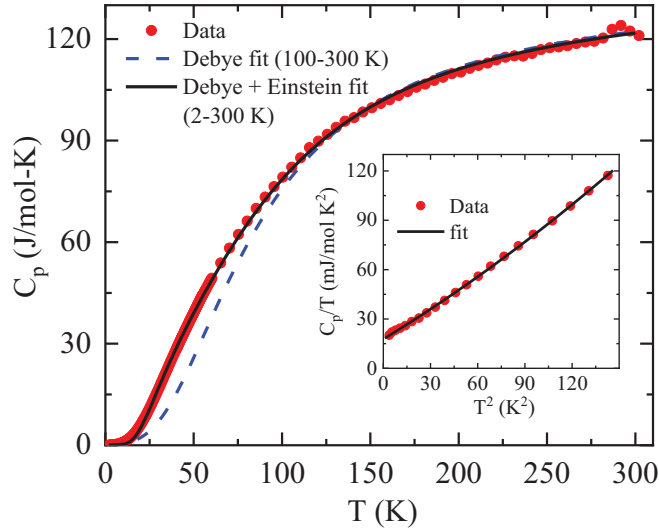


FIG. 7. Temperature T dependence of the zero-field heat capacity C_p for a SrCr₂As₂ single crystal. The bump in the data at ≈ 290 K is an experimental artifact. The data in the T range 100–300 K are fitted by the Debye model using Eq. (5) (dashed curve), whereas the data in the full T range 1.8–300 K are better described by a sum of Debye and Einstein contribution using Eq. (7) as shown by the solid curve in the figure. Inset: C_p/T vs T^2 at low temperatures along with a fit by Eq. (3) (solid curve).

The low- T $C_p(T)$ data for $1.8 \text{ K} \leq T \leq 12 \text{ K}$ were analyzed using the relation

$$C_p(T) = \gamma T + \beta T^3 + \delta T^5, \quad (3)$$

where γ is the Sommerfeld electronic heat-capacity coefficient and β and δ are coefficients associated with the low- T lattice heat-capacity contribution. The inset of Fig. 7 shows $C_p(T)/T$ versus T^2 along with the fit by Eq. (3). The fitted parameter values are $\gamma = 17.7(3) \text{ mJ/mol K}^2$, $\beta = 0.58(1) \text{ mJ/mol K}^4$, and $\delta = 0.8(1) \mu\text{J/mol K}^6$. The value of β was used to determine the Debye temperature Θ_D according to

$$\Theta_D = \left(\frac{12\pi^4 R n}{5\beta} \right)^{1/3} = 256(2) \text{ K}. \quad (4)$$

The $C_p(T)$ data for the full temperature range $1.8 \text{ K} \leq T \leq 300 \text{ K}$ were fitted by

$$C_p(T) = \gamma T + n C_{V \text{ Debye}}(T), \quad (5)$$

where the Debye lattice heat capacity at constant volume is given by

$$C_{V \text{ Debye}}(T) = 9R \left(\frac{T}{\Theta_D} \right)^3 \int_0^{\Theta_D/T} \frac{x^4 e^x}{(e^x - 1)^2} dx. \quad (6)$$

Here, we used $\gamma = 17.7 \text{ mJ/mol K}^2$ obtained from the above low- T data analysis and $C_{V \text{ Debye}}(T)$ was calculated using an accurate analytic Padé approximant function [37]. As seen from Fig. 7, the $C_p(T)$ data are only described by the Debye model in the temperature range 100–300 K with $\Theta_D = 342(2) \text{ K}$. This value of Θ_D is larger than the value of 256(2) K determined above from the fit of the $C_p(T)$ data at low T by Eq. (3).

A better fit to the $C_p(T)$ data over the full temperature range was obtained as the sum of the electronic and the Debye and Einstein lattice contributions

$$C_p(T) = \gamma T + (1 - \alpha) C_{V \text{ Debye}} + \alpha C_{V \text{ Einstein}}, \quad (7)$$

where

$$C_{V \text{ Einstein}}(T/\Theta_E) = 3R \left(\frac{\Theta_E}{T} \right)^2 \frac{e^{\Theta_E/T}}{(e^{\Theta_E/T} - 1)^2} \quad (8)$$

and Θ_E as the Einstein temperature. The relative fraction of the Debye and Einstein phonon contributions is determined by the parameter α . The best fit is obtained using the previous value $\gamma = 17.7 \text{ mJ/mol K}^2$, together with $\Theta_D = 434(3) \text{ K}$, $\Theta_E = 119(1) \text{ K}$, and $\alpha = 0.37(1)$ as shown by the solid black curve in Fig. 7. A similar value $\gamma = 19.3 \text{ mJ/mol K}^2$ has been reported for BaCr₂As₂ [38].

Now we estimate the density of states at the Fermi energy [$\mathcal{D}(E_F)$] from the value of $\gamma = 17.7 \text{ mJ/mol K}^2$. Using the relation $\gamma = \frac{1}{3} \pi^2 k_B^2 \mathcal{D}(E_F)$, $\mathcal{D}(E_F)$ is calculated to be 7.53 states/eV f.u. for both spin directions. From a comparison with a bare band-structure value of 3.7 states/eV f.u. for both spin directions obtained from a first-principles calculation [35], the effective mass of the carriers is suggested to be enhanced by a factor of ~ 2 in the AFM state of SrCr₂As₂. A similar enhancement has been pointed out in BaCr₂As₂ [38].

Finally it is noted that, in the present analysis, we did not include the magnetic contribution to the heat capacity. It is known that in the absence of an excitation energy gap, AFM spin waves at low temperatures have a T^3 heat-capacity dependence if the spin waves are three-dimensional (3D) and a T^2 dependence if two-dimensional. Since we have no information on the magnon dispersion relations, it was not possible to separate the contribution of spin waves from the contribution of the phonons to the βT^3 term in the low- T heat capacity, so by necessity we ignored a possible contribution of 3D spin waves to this term. However, in either 2D or 3D AFM spin waves, the presence would not affect the γT term in the heat capacity, which is the only term relevant to extracting the electronic contribution to the heat capacity.

D. Electrical resistivity measurements

Temperature-dependent electrical resistivity measurements were performed on several samples with current along the a direction in the plane, ρ_a . Measurements in the temperature range 1.8 to 400 K, performed on two different samples, were combined with measurements in the range 300 to 700 K, performed on two other samples. The curves for the samples were normalized by the value of the resistivity at room temperature, $\rho(300 \text{ K})$. The combined data are presented in the main panel of Fig. 8. The data in two different setups match smoothly in the range of overlap, 300 to 400 K. The $\rho_a(T)$ curve shows a metallic resistivity increase on warming in the whole temperature range up to 700 K. The $\rho_a(T)$ is linear in the paramagnetic state above T_N , and shows clear positive curvature below T_N . This resistivity behavior below T_N is typical for metals with contribution of spin-disorder scattering in the paramagnetic state [39].

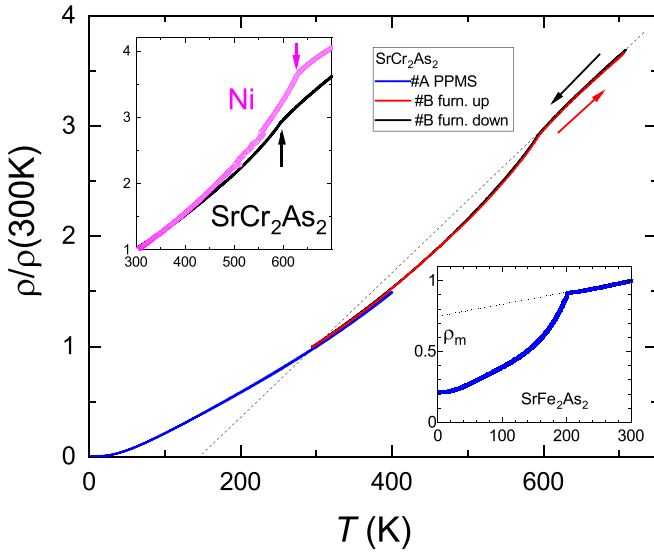


FIG. 8. In-plane electrical resistivity ρ_a of two samples of SrCr_2As_2 compiled from measurements in the PPMS (sample #A, 1.8 K to 400 K) and in the furnace set-up (#B, 300 K to 700 K). Measurements on sample #B were taken on warming (from 300 to 700 K, red curve and red arrow) and on cooling from 700 to 300 K (black curve and black arrow). The resistivity was normalized by the value at room temperature, $\rho(300\text{ K})$. This value was determined as $\rho_a(300\text{ K}) = 48 \pm 10\ \mu\Omega\text{ cm}$. The left inset compares high-temperature resistivity measurements of SrCr_2As_2 (black curve) with metallic Ni (magenta curve). The magenta and black arrows indicate the temperatures of the ferromagnetic transition in Ni and the antiferromagnetic transition in SrCr_2As_2 , respectively. The right inset shows the T dependence of the normalized $\rho_a/\rho(300\text{ K})$ for SrFe_2As_2 from Ref. [26]. The dashed line shows a linear extrapolation of the normalized $\rho(T)$ curve from above the transition to $T = 0$, showing the contribution of magnetic scattering in spin-disordered phase, similar to the main panel.

The data for SrCr_2As_2 are very similar to those in BaCr_2As_2 single crystals [17,19] and EuCr_2As_2 [40], though measurements in these compounds were not made to high enough temperatures to reach T_N . They also bear similarity to $\rho_a(T)/\rho(300\text{ K})$ for SrFe_2As_2 [26] (right inset of Fig. 8). In the case of SrFe_2As_2 , and as usual for magnetic scattering [41], the linear extrapolation of $\rho(T)$ curve above T_N to $T = 0$ gives a big positive offset on the resistivity axis. A similar extrapolation in SrCr_2As_2 (dashed line in the main panel of Fig. 8) gives a negative value, indicating a significantly stronger interaction of the charge carriers with the magnetic subsystem in the iron compounds.

Interestingly, the resistivity curve does not show any noticeable increase below T_N due to the appearance of magnetic superzone boundaries. This type of behavior is more common for ferromagnets. In the left inset of Fig. 8, we compare our measured electrical resistivity of ferromagnetic Ni with that of SrCr_2As_2 . Both samples show a clear downward deviation from the resistivity in the paramagnetic state. The derivative of the resistivity defines the ferromagnetic Curie temperature T_C of Ni as 630 K, in good agreement with a suggested value of 631 K [27]. In Ni there is no superzone boundary formation due to $Q = 0$ modulation in the ferromagnetic state. Super-

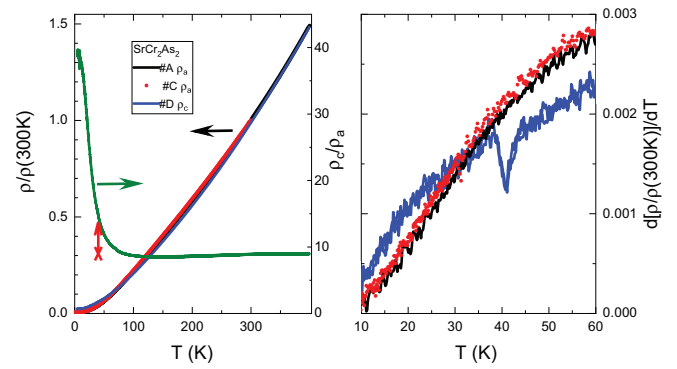


FIG. 9. The left panel compares the in-plane ρ_a (black and red curves for samples #A and #C), and interplane ρ_c (blue curve for sample #D) resistivity of SrCr_2As_2 . The black curve is slightly difficult to see due to the overlap with other two curves. The temperature dependence of the resistivity anisotropy ρ_c/ρ_a is also plotted by the green curve in the left panel. For a broad temperature range the anisotropy remains rather constant, but increases notably below 50 K. The red cross-arrow indicates the position of the anomaly in temperature-dependent resistivity derivative of $\rho_c(T)$ shown in the light panel where the temperature dependence of $d[\rho/\rho(300\text{ K})]/dT$ is plotted.

zone boundaries are formed at the points of electron energy bands crossing new magnetic Brillouin zone boundaries in the magnetically ordered state [39]. Modulation with a $Q = 0$ wave vector does not lead to a new periodicity in a ferromagnet, and as a result this effect is absent here. To understand the role of the magnetic superzone boundaries in SrCr_2As_2 , we refer to the band structure calculations [35,42], suggesting that the Fermi surface has the shape of a warped cylinder. This shape of the Fermi surface is indeed found experimentally in an ARPES study of the closely related BaCr_2As_2 [18]. The three-dimensional character of G-type magnetic ordering makes a poor match with the Fermi surface of this kind, with the magnetic Brillouin zone affecting very small areas of the Fermi surface. Compared with the small change of the density of states below T_N , clearly the loss of spin-disorder scattering provides a much bigger effect. Considering that the contribution of spin-disorder scattering vanishes with magnetic ordering, the curvature of the resistivity curve below T_N reflects mainly a build-up of the magnetic order parameter [see Fig. 10(d) below] and residual magnetic entropy [43].

In Fig. 9, we compare the in-plane ρ_a and interplane ρ_c resistivity of SrCr_2As_2 . The ρ_c data were taken in the two-probe mode. The measurements were made from 1.8 to 400 K. The interplane resistivity at room temperature was determined as $\rho_c(300\text{ K}) = 430 \pm 100\ \mu\Omega \cdot \text{cm}$. The resistivity anisotropy ρ_c/ρ_a is about 9 ± 2 at room temperature, and its temperature dependence is shown by the green curve in the left panel of Fig. 9 (the right axis). The anisotropy remains nearly constant down to 50 K, and then shows an about fourfold increase on further cooling. Interestingly, the onset of anisotropy increase correlates with a slight anomaly in the temperature dependence of the interplane resistivity derivative (see the right panel in Fig. 9). The origin of this anomaly remains unknown and it is not observed in other measurements.

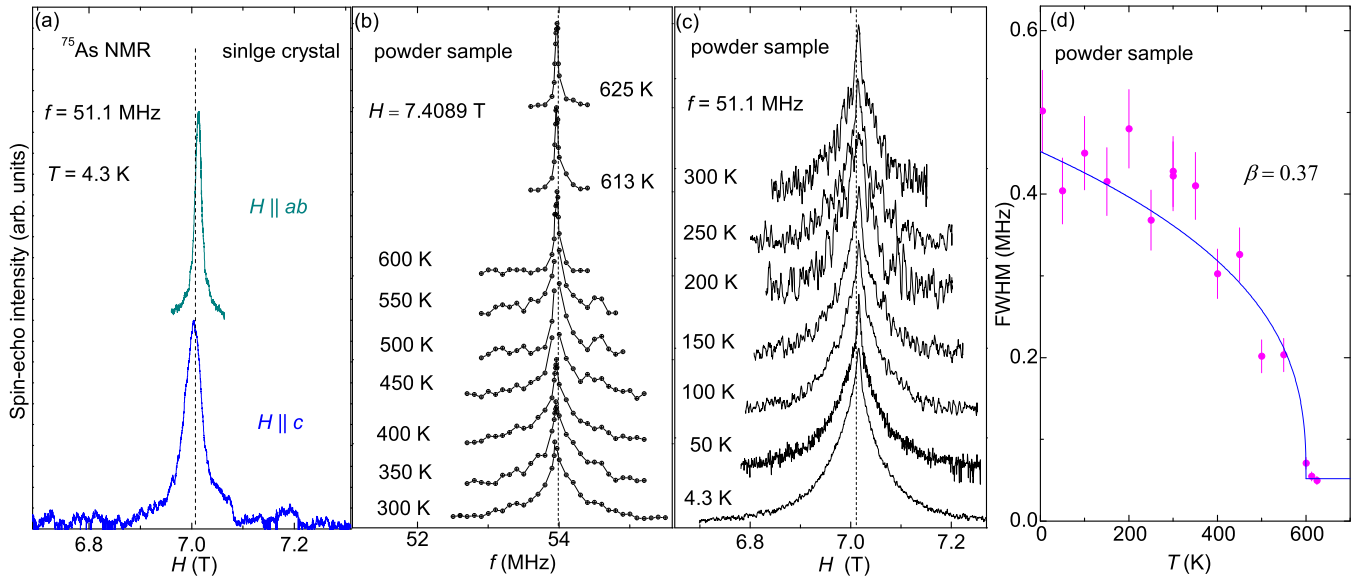


FIG. 10. (a) Field-swept ^{75}As -NMR spectra of a SrCr_2As_2 single crystal measured at $f = 51.1$ MHz and $T = 4.3$ K, for $H \parallel c$ axis and $H \parallel ab$ plane. The vertical dashed line represents the zero-shift position. (b) Temperature dependence of the f -swept ^{75}As -NMR spectrum for SrCr_2As_2 powder sample measured at $H = 7.4089$ T above $T = 300$ K. The vertical dashed line represents the zero-shift position. (c) Temperature dependence of the H -swept ^{75}As -NMR spectrum for a SrCr_2As_2 powder sample measured at $f = 51.1$ MHz below $T = 300$ K. The vertical dashed line represents the zero-shift position. (d) Temperature dependence of the FWHM of the ^{75}As -NMR spectrum for the SrCr_2As_2 powder sample. The solid line is calculated with $\text{FWHM}(T) = \text{FWHM}(0)(1 - T/T_N)^\beta + C$ where $\beta = 0.37$, $T_N = 600$ K, $\text{FWHM}(0) = 0.4$ MHz and $C = 0.052$ MHz.

E. NMR measurements

1. ^{75}As NMR spectra of SrCr_2As_2 single crystal

Figure 10(a) shows the field-swept ^{75}As -NMR spectra of a SrCr_2As_2 single crystal measured at frequency $f = 51.1$ MHz in the AFM state ($T = 4.3$ K) for $H \parallel c$ axis and $H \parallel ab$ plane. For the $I = 3/2$ nuclei, one may expect, in the presence of quadrupole effects, three spectral lines: one central ($I_z = 1/2 \leftrightarrow -1/2$) and two satellite transitions ($I_z = 3/2 \leftrightarrow 1/2$ and $-3/2 \leftrightarrow -1/2$). The observed ^{75}As -NMR spectra for both $H \parallel c$ axis and $H \parallel ab$ plane only show a single line around the Larmor field [dashed line in Fig. 10(a)]. The observation of the NMR line around the Larmor field indicates that there is no large internal magnetic field at the As site produced by the Cr ordered moments in the AFM state. The absence of clear satellite lines suggests that the quadrupolar interaction is quite small at the As site and we estimate the upper limit of the quadrupole interaction frequency ν_Q to be ≈ 0.1 MHz. The full width at half maximum (FWHM) of the line for $H \parallel c$ is ≈ 0.41 kOe which is greater than 0.16 kOe for $H \parallel ab$. No change in the peak positions and FWHMs were observed up to 100 K. Above 100 K, the NMR measurements on the single crystal became difficult due to weak signal intensity.

The internal field at the ^{75}As site can be analyzed by taking the crystal symmetry into consideration, which has been adopted in an analysis of the hyperfine field at the ^{75}As site in BaFe_2As_2 by Kitagawa *et al.* [44]. According to their analysis, for a G-type AFM spin structure, the internal field at the As site is zero due to a perfect cancellation of the off-diagonal hyperfine fields produced by four in-plane nearest-neighbor Cr spins when the spin moments are parallel to the c axis. Thus, the spin components along this axis do not produce any

shift in the ^{75}As NMR spectra. On the other hand, if there were ab plane components of the ordered Cr spin, they would produce an internal field perpendicular to the c axis at the ^{75}As site [44]. Thus one may expect the peak position to be shifted due to the internal field. However, according to the ND results, the AFM state is G-type where the Cr^{2+} ordered moments align along the c axis. Therefore, one expects a zero internal field at the As site in the AFM state of SrCr_2As_2 and should observe the NMR line around the Larmor field. This is consistent with what we observed in the ^{75}As NMR spectrum measurements, confirming the G-type AFM state in SrCr_2As_2 .

2. ^{75}As NMR spectra of SrCr_2As_2 powder sample

To overcome the difficulties for the NMR measurements at higher temperatures above 100 K with the SrCr_2As_2 single crystal, we used a polycrystalline sample which makes NMR measurements possible up to 625 K, which is above the Néel temperature. Figures 10(b) and 10(c) show the temperature dependence of the f -swept ^{75}As NMR spectrum of polycrystalline sample measured at $H = 7.4089$ T for $T \geq 300$ K, and the temperature dependence of the H -swept ^{75}As NMR spectrum measured at $f = 51.1$ MHz for $T \leq 300$ K, respectively. As in the case of the single crystal, a single peak expected for a small quadrupolar interaction was observed in the whole temperature range from 625 down to 4.3 K. Although no clear change in the peak position of the NMR spectra is observed, as the temperature decreases, the NMR spectra broaden below ≈ 600 K, which evidences the magnetic ordered state below this temperature.

Figure 10(d) shows the temperature dependence of the FWHM of the NMR spectra where the FWHM increases

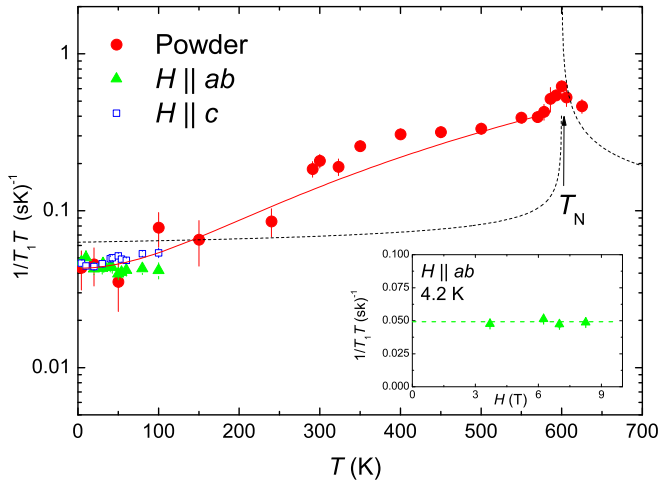


FIG. 11. Temperature dependence of the nuclear spin-lattice relaxation rate $1/T_1$ divided by T for both the SrCr_2As_2 single crystal and powder sample. The black dashed and red lines are the calculated results based on the SCR theory and the two-magnon scattering model, respectively (see text). Inset: Magnetic field dependence of $1/T_1 T$ at $T = 4.2$ K for $H \parallel ab$. The dashed horizontal line represents the average value.

gradually with decreasing temperature. Although the internal field at the As site is expected to be zero in the AFM state as described above, a distribution of the Cr ordered moments and/or distribution of the transferred hyperfine coupling constant would broaden the NMR spectra [45]. Since the temperature dependence of the FWHM for the NMR line in the case of polycrystalline samples in a magnetically ordered state reflects the temperature dependence of the order parameter (the magnitude of the Cr^{2+} ordered moments), the T dependence of the FWHM below 600 K indicates a second-order phase transition. In general, one can estimate a critical exponent for the AFM transition from the temperature dependence of the FWHM. However, our experimental data are somewhat scattered, so we do not estimate the critical exponent from our experimental data. Instead, we calculated the temperature dependence of the FWHM based on the ND measurements [20]. The solid curve in Fig. 10(d) is the calculated result of $\text{FWHM}(T) = \text{FWHM}(0)(1 - T/T_N)^\beta + C$ with $\beta = 0.37$ reported from the ND measurements. Here we used $\text{FWHM}(0) = 0.4$ MHz and $C = 0.052$ MHz which is the FWHM just above T_N . As shown, the curve with $\beta = 0.37$ reasonably reproduces the experimental data. Since the value of β is close to 0.33–0.367 for 3D Heisenberg, 0.31–0.345 for 3D XY, and 0.3–0.326 for 3D Ising models but much greater than 0.125 for the 2D Ising model [46], the results suggest a 3D nature of the magnetism in SrCr_2As_2 , as found from the ND measurements [20].

3. ^{75}As spin-lattice relaxation rate $1/T_1$

The AFM phase transition has also been detected from the ^{75}As spin-lattice relaxation rate ($1/T_1$) measurements. Figure 11 shows the temperature dependence of $1/T_1 T$ of the polycrystalline SrCr_2As_2 sample for $T = 4.2 - 625$ K, together with the $1/T_1 T$ results for the SrCr_2As_2 single crystal at low temperatures below 100 K for $H \parallel c$ axis and $H \parallel ab$

plane. $1/T_1 T$ increases as temperature decreases from 625 K, and shows a peak at $T_N \approx 600$ K, which is due to the critical slowing down of spin fluctuations for a second-order phase transition. Below T_N , with decreasing temperature, $1/T_1 T$ decreases gradually from 550 to 350 K, then shows a relatively steep decrease below 300 K and finally exhibits a $1/T_1 T = \text{constant}$ behavior below 100 K.

In the case of AFM metals, $1/T_1 T$ is given by

$$1/T_1 T = (1/T_1 T)_{\text{const}} + (1/T_1 T)_{\text{AFM}}, \quad (9)$$

where $(1/T_1 T)_{\text{const}}$ is the temperature-independent value originating from conduction carriers and the second term is due to AFM fluctuations. In the framework of weak itinerant antiferromagnets, the self-consistent renormalization (SCR) theory predicts the following relations [47]:

$$(1/T_1 T)_{\text{AFM}} = \frac{a}{\sqrt{(T - T_N)^{1/2}}} \quad (T > T_N) \quad (10)$$

$$= \frac{b}{M_Q(T)} \quad (T < T_N). \quad (11)$$

Here $M_Q(T)$ represents the temperature dependence of the staggered moments in the antiferromagnetic state. Although we tried to fit the data by changing the parameters, we were not able to reproduce the experimental data with the model. The typical results are shown by the black dashed lines in Fig. 11 calculated with the parameters $T_N = 600$ K, $a = 1.5$ $(\text{sK})^{-1}$, $b = 2 \times 10^{-2}$ $(\text{sK})^{-1}$ and $(1/T_1 T)_{\text{const}} = 0.043$ $(\text{sK})^{-1}$. Here we used the calculated $\text{FWHM}(T)$ as $M_Q(T)$. Then, we consider another possibility for $(1/T_1 T)_{\text{AFM}}$. When $1/T_1 T$ is mainly driven by scattering of magnons, often observed in antiferromagnetic insulators, $(1/T_1 T)_{\text{AFM}}$ is expected to follow a T^2 power-law temperature dependence due to a two-magnon Raman process [48]. The red solid line in Fig. 11 is the result calculated with $1/T_1 T = 0.043 + 1.2 \times 10^{-6} T^2$ $(\text{sK})^{-1}$, which reproduces the experimental data better than the fit with the SCR theory. A similar analysis of the temperature dependence of $1/T_1 T$ has been reported in the antiferromagnetic metal K-doped BaMn_2As_2 [49]. These results suggest that the nuclear relaxation process in the AFM state in the temperature region $T \sim 100$ –550 K mainly originates from magnon scattering and also suggest a relatively strong localized nature of the Cr ordered moments in the AFM state of SrCr_2As_2 . On the other hand, the T -independent $1/T_1 T = 0.043$ $(\text{sK})^{-1}$ observed below 100 K indicates that the nuclear relaxation in the temperature range is dominated by the relaxation process due to the conduction carriers, evidencing the metallic state from a microscopic point of view. The duality of localized and itinerant natures may originate from d electrons on the different $3d$ orbitals of the Cr ions in SrCr_2As_2 .

Since the T -independent $1/T_1 T$ observed at low temperatures is in general proportional to the square of the density of states at the Fermi level $\mathcal{D}(E_F)$ as [50] $(T_1 T)^{-1} = 4\pi \gamma_N^2 \hbar k_B A_{\text{hf}}^2 \mathcal{D}^2(E_F)$, where k_B is Boltzmann's constant and A_{hf} is a hyperfine coupling constant, these results indicate that $\mathcal{D}(E_F)$ is independent of temperature at least below 100 K. This is in contrast to the recent Raman spectroscopy measurements [21] which suggest a continuous decrease of the density of states at $T < 250$ K. Similar T -independent $1/T_1 T$ behaviors with $1/T_1 T \sim 0.043$ $(\text{sK})^{-1}$ are also observed in

the SrCr₂As₂ single crystal below ~ 100 K for two different magnetic field directions $H \parallel c$ axis and $H \parallel ab$, as shown in Fig. 11. These results again indicate the T -independent behavior of the $\mathcal{D}(E_F)$ below 100 K. In addition, the similar values of $1/T_1T$ for $H \parallel c$ and $H \parallel ab$ suggest no obvious anisotropy in the magnetic fluctuations due to conduction carriers in this material.

It is noted that we did not attribute the decrease in $1/T_1T$ from T_N to 100 K to the reduction of $\mathcal{D}(E_F)$. If the reduction of $1/T_1T$ from 0.2 (sK)⁻¹ at 300 K to 0.043 (sK)⁻¹ at 4 K is due to the reduction of $\mathcal{D}(E_F)$, the $\mathcal{D}(E_F)$ must be reduced by a factor of ≈ 2.2 at low temperatures since $1/T_1T$ is proportional to $\mathcal{D}^2(E_F)$. This seems to be inconsistent with the observed T dependence of χ_c and χ_{ab} . Assuming a Wilson ratio of 1, the Pauli paramagnetic susceptibility is estimated to be 2.43×10^{-4} cm³/mol from the Sommerfeld electronic heat-capacity coefficient $\gamma = 17.7$ mJ/mol K² (see Sec. III C). This corresponds to $\approx 32\%$ and $\approx 18\%$ of the observed χ_c and χ_{ab} , respectively, below 300 K. Therefore, although we do not know the origin of χ_c and χ_{ab} below T_N , one may expect to observe the change in χ_c and χ_{ab} if $\mathcal{D}(E_F)$ decreases with decreasing T . However, as shown in Fig. 3(c), the χ_c and χ_{ab} do not show an obvious reduction with decreasing T . These results indicate no obvious change in $\mathcal{D}(E_F)$ with decreasing T .

It is also important to point out that the Raman spectroscopy measurements suggested the reduction of $\mathcal{D}(E_F)$ with increasing magnetic field [21]. To check this possibility, we measured the H dependence of $1/T_1T$ at 4.2 K for $H \parallel ab$. As shown in the inset of Fig. 11, we found no obvious change in $1/T_1T$ from 3.7 T to 8.25 T, indicating that the $\mathcal{D}(E_F)$ is nearly independent of H up to 8.25 T.

4. ⁵³Cr zero-field NMR in the antiferromagnetic state

We tried to observe zero-field Cr-NMR signals in the single crystals, but no signals were detected. However, we succeeded in observing the ⁵³Cr-NMR signal under zero magnetic field in the SrCr₂As₂ powder sample at $T = 1.6$ K in the frequency range of $f \sim 59$ –82 MHz as shown in Fig. 12, although the signal intensity was very small due to a low natural 9.5% abundance of ⁵³Cr and the broad spectrum. This is direct evidence of the magnetic ordering of Cr moments in the AFM state. Since the signal intensity was very small even at the lowest temperature of 1.6 K, it is hard to measure the spectrum precisely, making analysis of the spectrum difficult. Nevertheless, we tried to fit the spectrum. The green curve in Fig. 12 is the calculated ⁵³Cr-NMR spectrum with a set of parameters of the internal magnetic field at the Cr site $|H_{\text{int}}^{\text{Cr}}| = 29.5$ T, Cr quadrupolar interaction frequency $\nu_Q = 8$ MHz, and $\theta = 0$. Here θ represents the angle between $H_{\text{int}}^{\text{Cr}}$ and the principle axis of the EFG tensor at the Cr sites. Since the Cr site has a local fourfold symmetry around the c axis in the tetragonal ThCr₂Si₂-type crystal structure, the principal axis of the EFG at the Cr site is parallel to the c axis. Therefore, since the Cr ordered moments align along the c axis under zero magnetic field from the ND measurements [20], we used $\theta = 0$ for the simulation. As shown in Fig. 12, the observed spectrum was not reproduced well by the simulated spectrum, so we are not

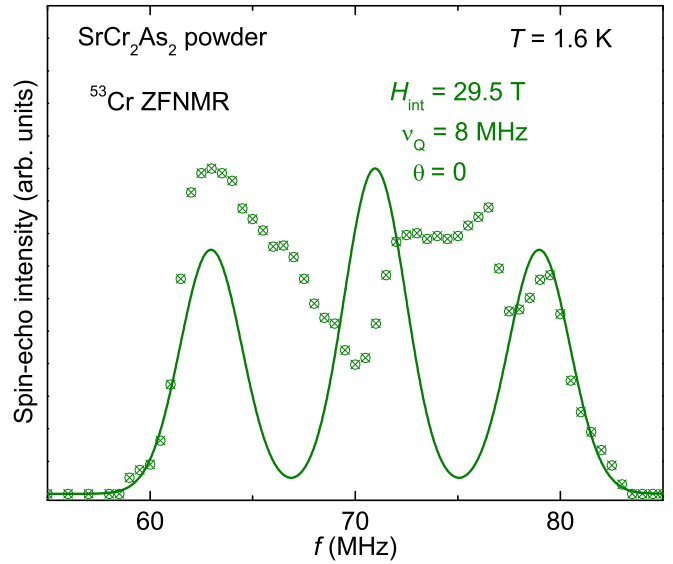


FIG. 12. Zero-field ⁵³Cr NMR spectrum at $T = 1.6$ K. The green curve is the calculated ⁵³Cr-NMR spectrum using the parameters $B_{\text{int}}^{\text{Cr}} = 29.5$ T, $\nu_Q = 8$ MHz, and $\theta = 0$.

able to discuss much about the parameters obtained from the simulation.

However, we consider that the frequency range we observed ⁵³Cr-NMR signals provides some information about the magnitude of the Cr ordered moments. In general, the ⁵³Cr-NMR resonance frequency in magnetic materials is closely related to the total spin value of the $3d$ electrons on Cr ions since the resonance frequency is proportional to $H_{\text{int}}^{\text{Cr}}$ which is proportional to the Cr ordered moments $\langle \mu \rangle$ via the hyperfine interaction. Therefore, one may observe ⁵³Cr NMR in different frequency ranges with different ionic states of Cr ions. For example, ⁵³Cr-NMR signals for Cr⁴⁺ with $S = 1$ ($3d^2$) in the FM half-metal CrO₂ are observed around $f = 26$ –37 MHz [51–53], while the signals are located around 65–70 MHz for Cr³⁺ with $S = 3/2$ ($3d^3$) in insulating antiferromagnets Cr₂O₃ [53,54], YCrO₃ [53,55] and CuCrO₂ [56]. ⁵³Cr-NMR signals were also observed around 44–57 MHz for $\langle \mu \rangle = 0.76$ –0.97 μ_B in Cr-based molecular rings [57]. Therefore, the resonance frequency $f = 59$ –80 MHz observed in SrCr₂As₂ suggests that the Cr ordered moments have spin $\lesssim S = 3/2$ ($\mu = 3 \mu_B$). This is less than the value of 4 μ_B expected for Cr²⁺ ($S = 2$) ions in localized systems, which is consistent with the itinerant nature of the antiferromagnetism in SrCr₂As₂. The hyperfine coupling constants for Cr ions have been reported to be $A_{\text{hf}} = -11.7$ to -12.7 T/ μ_B in Cr-based magnetic compounds [55,58]. Using $H_{\text{int}}^{\text{Cr}} = 29.5$ T and $\langle \mu \rangle = 1.9 \mu_B/\text{Cr}$ and 2.26–2.4 μ_B/Cr from the ND measurements [20] and the first-principles density-functional calculations [35,42], respectively, $|A_{\text{hf}}| = H_{\text{int}}^{\text{Cr}}/\langle \mu \rangle$ is estimated to be 15.5 T/ μ_B and 12.3 to 13.1 T/ μ_B , respectively. Although $|A_{\text{hf}}| = 15.5$ T/ μ_B is slightly greater than the reported value, $|A_{\text{hf}}| = 12.3$ to 13.1 T/ μ_B is reasonably close to it. These results indicate reduced ordered moments of Cr ions compared to the above local-moment value of 4 μ_B/Cr in SrCr₂As₂.

IV. SUMMARY

The electronic and magnetic properties of itinerant antiferromagnetic SrCr_2As_2 with single crystalline and polycrystalline forms have been studied by a variety of measurements including electrical resistivity ρ , heat capacity C_p , magnetic susceptibility χ versus temperature T and magnetization M versus applied magnetic field H isotherm measurements from a macroscopic point of view as well as ^{75}As and ^{53}Cr NMR measurements from a microscopic point of view in a wide temperature range of $T = 1.6\text{--}900$ K.

The metallic ground state was directly evidenced by the electrical-resistivity and heat-capacity measurements as well as NMR measurements. From the value of the Sommerfeld coefficient of the electronic heat capacity $\gamma = 17.7$ mJ/mol K^2 , the density of states at Fermi energy $\mathcal{D}(E_F)$ in the AFM state is estimated to be 7.53 states/eV f.u. for both spin directions, which is almost twice the bare $\mathcal{D}(E_F)$ estimated from first-principles calculations, suggesting an enhancement of the conduction carrier mass by a factor of two in the AFM state. In addition, the temperature and magnetic-field dependences of the ^{75}As spin-lattice relaxation rate divided by T , $1/T_1T$, at low temperatures indicate that the $\mathcal{D}(E_F)$ is nearly constant at least below 100 K and is independent of H up to 8.25 T, in contrast to the recent report from the Raman spectroscopy measurements [21] which suggest a continuous decrease of the $\mathcal{D}(E_F)$ below $T < 250$ K and also with increasing H .

The $\rho(T)$ is found to show T -linear behavior above T_N and exhibits positive curvature below T_N where significant loss of spin-disorder scattering upon magnetic ordering is observed. The T dependence of $\rho(T)$ is found to bear some similarity to the parent compounds of iron-based superconductors BaFe_2As_2 and SrFe_2As_2 , but not CaFe_2As_2 [26]. The resistivity anisotropy of the compound remains moderate $\rho_c/\rho_a \sim 9$

through most of the magnetically ordered phase but shows rapid increase below 50 K.

The AFM ordering temperature $T_N = 615(15)$ K has been detected from a clear peak in $d(\chi T)/dT$, a slope discontinuity in $\rho(T)$, a sudden change in ^{75}As NMR line width and also a peak in the T dependence of $1/T_1$. The observation of the ^{75}As NMR spectrum around the zero-shift position (Larmor field) for both single-crystal and powder samples in the AFM state below T_N indicates a G-type AFM spin structure. From the $\chi(T)$ measurements on SrCr_2As_2 single crystal under the two different magnetic field directions $H \parallel ab$ and $H \parallel c$ in the AFM state, the Cr ordered moments are shown to align along the c axis in the G-type AFM state, consistent with the results from the previous neutron-diffraction measurements. The temperature dependence of $1/T_1$ in the AFM state cannot be reproduced by the SCR theory for weak itinerant antiferromagnets, but it was found that a magnon-scattering model often observed in antiferromagnetic insulators roughly reproduces the experimental data. The result suggests the localized nature of the Cr ordered moments in the metallic AFM state of SrCr_2As_2 , showing the duality of localized and itinerant natures which could originate from d electrons on the different $3d$ orbitals of the Cr ions. Further detailed studies are required for understanding the role of each electron of the $3d$ orbitals of the Cr^{2+} ions as well as the origin of the dual nature, which leads to deeper understandings of the electron correlations in SrCr_2As_2 and also in the other Cr-based compounds.

ACKNOWLEDGMENTS

This research was supported by the U.S. Department of Energy, Office of Basic Energy Sciences, Division of Materials Sciences and Engineering. Ames Laboratory is operated for the U.S. Department of Energy by Iowa State University under Contract No. DE-AC02-07CH11358.

- [1] Y. Kamihara, T. Watanabe, M. Hirano, and H. Hosono, Iron-based layered superconductor $\text{La}[\text{O}_{1-x}\text{F}_x]\text{FeAs}$ ($x = 0.05\text{--}0.12$) with $T_c = 26$ K, *J. Am. Chem. Soc.* **130**, 3296 (2008).
- [2] D. C. Johnston, The puzzle of high temperature superconductivity in layered iron pnictides and chalcogenides, *Adv. Phys.* **59**, 803 (2010).
- [3] P. C. Canfield and S. L. Bud'ko, FeAs-based superconductivity: A case study of the effects of transition metal doping on BaFe_2As_2 , *Annu. Rev. Condens. Matter Phys.* **1**, 27 (2010).
- [4] G. R. Stewart, Superconductivity in iron compounds, *Rev. Mod. Phys.* **83**, 1589 (2011).
- [5] Y. Singh, M. A. Green, Q. Huang, A. Kreyssig, R. J. McQueeney, D. C. Johnston, and A. I. Goldman, Magnetic order in BaMn_2As_2 from neutron diffraction measurements, *Phys. Rev. B* **80**, 100403(R) (2009).
- [6] D. C. Johnston, R. J. McQueeney, B. Lake, A. Honecker, M. E. Zhitomirsky, R. Nath, Y. Furukawa, V. P. Antropov, and Y. Singh, Magnetic exchange interactions in BaMn_2As_2 : A case study of the $J_1\text{--}J_2\text{--}J_c$ Heisenberg model, *Phys. Rev. B* **84**, 094445 (2011).
- [7] W.-S. Wang, M. Gao, Y. Yang, Y.-Y. Xiang, and Q.-H. Wang, Possible superconductivity in the electron-doped chromium pnictide LaOCrAs , *Phys. Rev. B* **95**, 144507 (2017).
- [8] J. M. Pizarro, M. J. Calderón, J. Liu, M. C. Muñoz, and E. Bascones, Strong correlations and the search for high- T_c superconductivity in chromium pnictides and chalcogenides, *Phys. Rev. B* **95**, 075115 (2017).
- [9] M. Edelmann, G. Sangiovanni, M. Capone, and L. de' Medici, Chromium analogs of iron-based superconductors, *Phys. Rev. B* **95**, 205118 (2017).
- [10] W. Wu, J. Cheng, K. Matsubayashi, P. Kong, F. Lin, C. Jin, N. Wang, Y. Uwatoko, and J. Luo, Superconductivity in the vicinity of antiferromagnetic order in CrAs , *Nat. Commun.* **5**, 5508 (2014).
- [11] H. Kotegawa, S. Nakahara, H. Tou, and H. Sugawara, Superconductivity of 2.2 K under pressure in helimagnet CrAs , *J. Phys. Soc. Jpn.* **83**, 093702 (2014).
- [12] J. K. Bao, J. Y. Liu, C. W. Ma, Z. H. Meng, Z. T. Tang, Y. L. Sun, H. F. Zhai, H. Jiang, H. Bai, C. M. Feng, Z. A. Xu, and G. H. Cao, Superconductivity in Quasi-One-Dimensional $\text{K}_2\text{Cr}_3\text{As}_3$ with Significant Electron Correlations, *Phys. Rev. X* **5**, 011013 (2015).
- [13] Z.-T. Tang, J.-K. Bao, Y. Liu, Y.-L. Sun, A. Ablimit, H.-F. Zhai, H. Jiang, C.-M. Feng, Z.-A. Xu, and G.-H. Cao, Unconventional superconductivity in quasi-one-dimensional $\text{Rb}_2\text{Cr}_3\text{As}_3$, *Phys. Rev. B* **91**, 020506(R) (2015).

- [14] Z. T. Tang, J. K. Bao, Z. Wang, H. Bai, H. Jiang, Y. Liu, H. F. Zhai, C. M. Feng, Z. A. Xu, and G. H. Cao, Superconductivity in quasi-one-dimensional $\text{Cs}_2\text{Cr}_3\text{As}_3$ with large interchain distance, *Sci. China Mater.* **58**, 16 (2015).
- [15] Q. G. Mu, B. B. Ruan, B. J. Pan, T. Liu, J. Yu, K. Zhao, G. F. Chen, and Z. A. Ren, Ion-exchange synthesis and superconductivity at 8.6 K of $\text{Na}_2\text{Cr}_3\text{As}_3$ with quasi-one-dimensional crystal structure, *Phys. Rev. Mater.* **2**, 034803 (2018).
- [16] Z.-T. Tang, J.-K. Bao, Y. Liu, H. Bai, H. Jiang, H.-F. Zhai, C.-M. Feng, Z.-A. Xu, and G.-H. Cao, Synthesis, crystal structure and physical properties of quasi-one-dimensional ACr_3As_3 ($A = \text{Rb}, \text{Cs}$), *Sci. China Mater.* **58**, 543 (2015).
- [17] K. A. Filsinger, W. Schnelle, P. Adler, G. H. Fecher, M. Reehuis, A. Hoser, J.-U. Hoffmann, P. Werner, M. Greenblatt, and C. Felser, Antiferromagnetic structure and electronic properties of BaCr_2As_2 and BaCrFeAs_2 , *Phys. Rev. B* **95**, 184414 (2017).
- [18] J. Nayak, K. Filsinger, G. H. Fecher, S. Chadov, J. Minár, E. D. L. Rienks, B. Büchner, S. P. Parkin, J. Fink, and C. Felser, Observation of a remarkable reduction of correlation effects in BaCr_2As_2 by ARPES, *Proc. Natl. Acad. Sci. USA* **114**, 12425 (2017).
- [19] P. Richard, A. van Roekeghem, B. Q. Lv, T. Qian, T. K. Kim, M. Hoesch, J.-P. Hu, A. S. Sefat, S. Biermann, and H. Ding, Is BaCr_2As_2 symmetrical to BaFe_2As_2 with respect to half $3d$ shell filling? *Phys. Rev. B* **95**, 184516 (2017).
- [20] P. Das, N. S. Sangeetha, G. R. Lindemann, T. W. Heitmann, A. Kreyssig, A. I. Goldman, R. J. McQueeney, D. C. Johnston, and D. Vaknin, Itinerant G-type antiferromagnetic order in SrCr_2As_2 , *Phys. Rev. B* **96**, 014411 (2017).
- [21] U. F. Kaneko, M. D. Teodoro, P. F. Gomes, N. S. Sangeetha, and D. C. Johnston, Electron-phonon coupling enhancement and displacive magnetostructural transition in SrCr_2As_2 under magneto-Raman spectroscopy, *J. Phys.: Condens. Matter* **33**, 105401 (2021).
- [22] J. Rodríguez-Carvajal, Recent advances in magnetic structure determination by neutron powder diffraction, *Phys. B* **192**, 55 (1993).
- [23] M. A. Tanatar, N. Ni, C. Martin, R. T. Gordon, H. Kim, V. G. Kogan, G. D. Samolyuk, S. L. Bud'ko, P. C. Canfield, and R. Prozorov, Anisotropy of the iron pnictide superconductor $\text{Ba}(\text{Fe}_{1-x}\text{Co}_x)_2\text{As}_2$ ($x = 0.074$, $T_c = 23$ K), *Phys. Rev. B* **79**, 094507 (2009).
- [24] M. A. Tanatar, N. Ni, S. L. Bud'ko, P. C. Canfield, and R. Prozorov, Field-dependent transport critical current in single crystals of $\text{Ba}(\text{Fe}_{1-x}\text{TM}_x)_2\text{As}_2$ ($\text{TM} = \text{Co}, \text{Ni}$) superconductors, *Supercond. Sci. Technol.* **23**, 054002 (2010).
- [25] M. A. Tanatar, R. Prozorov, N. Ni, S. L. Bud'ko, and P. C. Canfield, Low Resistivity Contact to Iron-Pnictide Superconductors, U. S. Patent **8**, 450, 246 (2011).
- [26] M. A. Tanatar, N. Ni, G. D. Samolyuk, S. L. Bud'ko, P. C. Canfield, and R. Prozorov, Resistivity anisotropy of AFe_2As_2 ($A = \text{Ca}, \text{Sr}, \text{Ba}$): Direct versus Montgomery technique measurements, *Phys. Rev. B* **79**, 134528 (2009).
- [27] B. Legendre and M. Sghaier, Curie temperature of nickel, *J. Therm. Anal. Calorim.* **105**, 141 (2011).
- [28] M. Pfisterer and G. Nagorsen, On the structure of ternary arsenides, *Z. Naturforsch.* **35b**, 703 (1980).
- [29] W. Wu, X.-D. Zhang, Z.-H. Yin, P. Zheng, N.-L. Wang, and J.-L. Luo, Low temperature properties of pnictide CrAs single crystal, *Sci. China* **53**, 1207 (2010).
- [30] X. Zhu, L. Ling, Y. Han, J. Xu, Y. Wang, H. Zhang, C. Zhang, L. Pi, and Y. Zhang, Single crystal growth of the new pressure-induced-superconductor CrAs via chemical vapor transport, *J. Alloys Compd.* **677**, 57 (2016).
- [31] M. E. Fisher, Relation between the specific heat and susceptibility of an antiferromagnet, *Philos. Mag.* **7**, 1731 (1962).
- [32] N. S. Sangeetha, A. Pandey, Z. A. Benson, and D. C. Johnston, Strong magnetic correlations to 900 K in single crystals of the trigonal antiferromagnetic insulators SrMn_2As_2 and CaMn_2As_2 , *Phys. Rev. B* **94**, 094417 (2016).
- [33] N. S. Sangeetha, V. Smetana, A.-V. Mudring, and D. C. Johnston, Antiferromagnetism in semiconducting SrMn_2Sb_2 and BaMn_2As_2 single crystals, *Phys. Rev. B* **97**, 014402 (2018).
- [34] N. S. Sangeetha, S. Pakhira, Q.-P. Ding, H.-C. Lee, V. Smetana, A.-V. Mudring, Y. Furukawa, and D. C. Johnston, First-order transitions at the Néel temperatures of trigonal SrMn_2P_2 and CaMn_2P_2 single crystals containing corrugated-honeycomb Mn sublattices, *Proc. Nat. Acad. Sci. USA* **118**, e2108724118 (2021).
- [35] W. Zhou, P. Hu, S. Li, and S. Wu, First-principles study of the magnetic and electronic properties of ACr_2As_2 ($A = \text{Sr}, \text{Ba}$), *J. Magn. Magn. Mater.* **476**, 254 (2019).
- [36] D. C. Johnston, Magnetic dipole interactions in crystals, *Phys. Rev. B* **93**, 014421 (2016).
- [37] R. J. Goetsch, V. K. Anand, A. Pandey, and D. C. Johnston, Structural, thermal, magnetic, and electronic transport properties of the $\text{LaNi}_2(\text{Ge}_{1-x}\text{P}_x)_2$ system, *Phys. Rev. B* **85**, 054517 (2012).
- [38] D. J. Singh, A. S. Sefat, M. A. McGuire, B. C. Sales, D. Mandrus, L. H. VanBebber, and V. Keppens, Itinerant antiferromagnetism in BaCr_2As_2 : Experimental characterization and electronic structure calculations, *Phys. Rev. B* **79**, 094429 (2009).
- [39] M. D. Wilding and E. W. Lee, Superzone boundary effects in the electrical resistivity of dysprosium, *Proc. Phys. Soc. Lond.* **85**, 955 (1965).
- [40] U. B. Paramanik, R. Prasad, C. Geibel, and Z. Hossain, Itinerant and local-moment magnetism in EuCr_2As_2 single crystals, *Phys. Rev. B* **89**, 144423 (2014).
- [41] B. R. Coles, Spin-disorder effects in the electrical resistivity of metals and alloys, *Adv. Phys.* **7**, 40 (1958).
- [42] A. K. Hamri, M. Djermouni, A. Zaoui, and S. Kacim, *Ab-initio* study of the electronic structure and magnetic properties of ACr_2Pn_2 ($A = \text{Ba}, \text{Sr}, \text{Ca}, \text{Sc}, \text{K}$; $\text{Pn} = \text{As}, \text{P}$), *J. Phys. Chem. Solids* **150**, 109850 (2021).
- [43] J. Paglione, M. A. Tanatar, D. G. Hawthorn, R. W. Hill, F. Ronning, M. Sutherland, L. Taillefer, C. Petrovic, and P. C. Canfield, Heat Transport as a Probe of Electron Scattering by Spin Fluctuations: The Case of Antiferromagnetic CeRhIn_5 , *Phys. Rev. Lett.* **94**, 216602 (2005).
- [44] K. Kitagawa, N. Katayama, K. Ohgushi, M. Yoshida, and M. Takigawa, Commensurate Itinerant antiferromagnetism in BaFe_2As_2 : ^{75}As -NMR studies on a self-flux grown single crystal, *J. Phys. Soc. Jpn.* **77**, 114709 (2008).

- [45] For example, Q.-P. Ding, W. R. Meier, A. E. Böhmer, S. L. Bud'ko, P. C. Canfield, and Y. Furukawa, NMR study of the new magnetic superconductor $\text{CaK}(\text{Fe}_{0.951}\text{Ni}_{0.049})_4\text{As}_4$: Microscopic coexistence of hedgehog spin-vortex crystal and superconductivity, *Phys. Rev. B* **96**, 220510(R) (2017).
- [46] R. Nath, Y. Furukawa, F. Borsa, E. E. Kaul, M. Baenitz, C. Geibel, and D. C. Johnston, Single-crystal ^{31}P NMR studies of the frustrated square-lattice compound $\text{Pb}_2(\text{VO})(\text{PO}_4)_2$, *Phys. Rev. B* **80**, 214430 (2009) and references therein.
- [47] T. Moriya and K. Ueda, Nuclear magnetic relaxation in weakly ferro- and antiferromagnetic metals, *Solid State Commun.* **15**, 169 (1974).
- [48] D. Beeman and P. Pincus, Nuclear spin-lattice relaxation in magnetic insulators, *Phys. Rev.* **166**, 359 (1968).
- [49] S. Yeninas, Abhishek Pandey, V. Ogloblichev, K. Mikhalev, D. C. Johnston, and Y. Furukawa, Metal-insulator transition in antiferromagnetic $\text{Ba}_{1-x}\text{K}_x\text{Mn}_2\text{As}_2$ ($0 \leq x \leq 0.4$) single crystals studied by ^{55}Mn and ^{75}As NMR, *Phys. Rev. B* **88**, 241111(R) (2013).
- [50] A. Narath, in *Hyperfine Interactions*, edited by A. J. Freeman and R. B. Frankel (Academic Press, New York, 1967), pp. 287–361.
- [51] H. Nishihara, T. Tsuda, A. Hirai, and T. Shinjo, Nuclear magnetic resonance of Cr^{53} in ferromagnetic CrO_2 , *J. Phys. Soc. Jpn.* **32**, 85 (1972).
- [52] J. H. Shim, S. Lee, J. Dho, and D.-H. Kim, Coexistence of Two Different Cr Ions by Self-Doping in Half-Metallic CrO_2 Nanorods, *Phys. Rev. Lett.* **99**, 057209 (2007).
- [53] H. Takeda, Y. Shimizu, M. Itoh, M. Isobe, and Y. Ueda, Local electronic state in the high-valence hollandite-type chromium oxide $\text{K}_2\text{Cr}_8\text{O}_{16}$ investigated by ^{53}Cr NMR, *Phys. Rev. B* **88**, 165107 (2013).
- [54] M. Rubinstein, G. H. Stauss, and J. J. Krebs, Nuclear magnetic resonance of Cr^{53} in antiferromagnetic Cr_2O_3 , *Phys. Lett.* **12**, 302 (1964).
- [55] E. Jedryka, S. Nadolski, and M. Wojcik, Wall NMR in the weak ferromagnets YCrO_3 and LuCrO_3 , *J. Magn. Magn. Mater.* **40**, 303 (1984).
- [56] A. G. Smolnikov, V. V. Ogloblichev, S. V. Verkhovskii, K. N. Mikhalev, A. Yu. Yakubovskii, K. Kumagai, Y. Furukawa, A. F. Sadykov, Yu. V. Piskunov, A. P. Gerashchenko, S. N. Barilo, and S. V. Shiryaev, ^{53}Cr NMR study of CuCrO_2 multiferroic, *J. Exp. Theor. Phys. Lett.* **102**, 674 (2015).
- [57] E. Micotti, Y. Furukawa, K. Kumagai, S. Carretta, A. Lascialfari, F. Borsa, G. A. Timco, and R. E. P. Winpenny, Local Spin Moment Distribution in Antiferromagnetic Molecular Rings Probed by NMR, *Phys. Rev. Lett.* **97**, 267204 (2006).
- [58] E. Garlatti, G. Allodi, S. Bordignon, L. Bordonali, G. A. Timco, R. E. P. Winpenny, A. Lascialfari, R. De Renzi, and S. Carretta, Breaking the ring: ^{53}Cr -NMR on the Cr_8Cd molecular nanomagnet, *J. Phys.: Condens. Matter* **32**, 244003 (2020).